


## Article

# S-Scheme BiOCl/MoSe<sub>2</sub> Heterostructure with Enhanced Photocatalytic Activity for Dyes and Antibiotics Degradation under Sunlight Irradiation

Yan Huang<sup>1,2</sup>, Fan Chen<sup>1</sup>, Zhipeng Guan<sup>1</sup>, Yusheng Luo<sup>1</sup>, Liang Zhou<sup>3</sup>, Yufeng Lu<sup>1</sup>, Baozhu Tian<sup>1,4,\*</sup>   
and Jinlong Zhang<sup>1,\*</sup>

- <sup>1</sup> Key Laboratory for Advanced Materials and Feringa Nobel Prize Scientist Joint Research Center, Institute of Fine Chemicals, School of Chemistry and Molecular Engineering, East China University of Science and Technology, 130 Meilong Road, Shanghai 200237, China; huangyan\_135@126.com (Y.H.); avazaza0131@icloud.com (F.C.); guan10130725@126.com (Z.G.); lyslouis217@126.com (Y.L.); luyufenghd@163.com (Y.L.)
- <sup>2</sup> Research Institute of Physical and Chemical Engineering of Nuclear Industry, 168 Jintang Road, Tianjin 300180, China
- <sup>3</sup> State Environmental Protection Key Lab of Environmental Risk Assessment and Control on Chemical Processes, School of Resources & Environmental Engineering, East China University of Science and Technology, 130 Meilong Road, Shanghai 200237, China; zhouliang@ecust.edu.cn
- <sup>4</sup> Key Laboratory of Specially Functional Polymeric Materials and Related Technology (Ministry of Education), East China University of Science and Technology, 130 Meilong Road, Shanghai 200237, China
- \* Correspondence: baozhutian@ecust.edu.cn (B.T.); jlzhang@ecust.edu.cn (J.Z.);  
Tel.: +86-21-64252062 (B.T. & J.Z.)



**Citation:** Huang, Y.; Chen, F.; Guan, Z.; Luo, Y.; Zhou, L.; Lu, Y.; Tian, B.; Zhang, J. S-Scheme BiOCl/MoSe<sub>2</sub> Heterostructure with Enhanced Photocatalytic Activity for Dyes and Antibiotics Degradation under Sunlight Irradiation. *Sensors* **2022**, *22*, 3344. <https://doi.org/10.3390/s22093344>

Academic Editor: Chris Blackman

Received: 31 March 2022

Accepted: 25 April 2022

Published: 27 April 2022

**Publisher's Note:** MDPI stays neutral with regard to jurisdictional claims in published maps and institutional affiliations.



**Copyright:** © 2022 by the authors. Licensee MDPI, Basel, Switzerland. This article is an open access article distributed under the terms and conditions of the Creative Commons Attribution (CC BY) license (<https://creativecommons.org/licenses/by/4.0/>).

**Abstract:** Semiconductor photocatalysis is considered to be a promising technique to completely eliminate the organic pollutants in wastewater. Recently, S-scheme heterojunction photocatalysts have received much attention due to their high solar efficiency, superior transfer efficiency of charge carriers, and strong redox ability. Herein, we fabricated an S-scheme heterostructure BiOCl/MoSe<sub>2</sub> by loading MoSe<sub>2</sub> nanosheets on the surface of BiOCl microcrystals, using a solvothermal method. The microstructures, light absorption, and photoelectrochemical performances of the samples were characterized by the means of SEM, TEM, XRD, transient photocurrents, electrochemical impedance, and photoluminescence (PL) spectra. The photocatalytic activities of BiOCl, MoSe<sub>2</sub>, and the BiOCl/MoSe<sub>2</sub> samples with different MoSe<sub>2</sub> contents were evaluated by the degradation of methyl orange (MO) and antibiotic sulfadiazine (SD) under simulated sunlight irradiation. It was found that BiOCl/MoSe<sub>2</sub> displayed an evidently enhanced photocatalytic activity compared to single BiOCl and MoSe<sub>2</sub>, and 30 wt.% was an optimal loading amount for obtaining the highest photocatalytic activity. On the basis of radical trapping experiments and energy level analyses, it was deduced that BiOCl/MoSe<sub>2</sub> follows an S-scheme charge transfer pathway and •O<sub>2</sub><sup>-</sup>, •OH, and h<sup>+</sup> all take part in the degradation of organic pollutants.

**Keywords:** photocatalysis; dye; antibiotics; S-scheme heterojunction; photocatalytic activity; reactive species; organic pollutant

## 1. Introduction

With the rapid development of urbanization and industrialization, water pollution has become more and more serious and imparted huge adverse effects on aquatic ecosystems, human health, and the development of economy and society [1–3]. In recent decades, the removal of noxious organic pollutants in wastewater, such as drugs [4,5], dyes [6,7], and antibiotics [8], has become a big challenge that must be managed. For instance, the antibiotics always bring about side effects on ecosystems and human health by inducing the proliferation of bacterial drug resistance [6]. The carcinogenic and teratogenic dyes can

enter the human body along with the polluted water, leading to the appearance of cancers and other serious illnesses. To eliminate these organic pollutants, a series of techniques, such as physical adsorption, micro-biological degradation, and chemical oxidation, have been applied in the remediation of organic pollutants [1,9]. However, these strategies are still insufficient to completely remove the water-borne organic pollutants because of their low efficiency, as well as the formation of secondary waste products [10–12]. Alternatively, semiconductor photocatalysis has received much attention as a promising solution to completely eliminate the organic contaminants in wastewater [1–7,13–19]. As a semiconductor with wide bandgap, BiOCl is considered to be an ideal photocatalyst for the decomposition of organic pollutants in wastewater under UV light [20,21]. The main weakness of BiOCl is that it cannot respond to visible light, severely blocking its application in the whole solar spectrum. To solve this problem, the researchers have developed many strategies, such as fabricating oxygen vacancies, depositing with metals, constructing heterojunctions, and so on [22–30]. Although these approaches can extend the light response of BiOCl to the visible region, they inevitably decrease the redox ability of the photogenerated electrons and holes. In this regard, the researchers further exploited a series of all-solid-state and direct Z-scheme composite semiconductors to avoid decreasing the redox ability of photogenerated charge carriers [13,14,31–38]. Recently, Yu et al. proposed a novel S-scheme heterojunction theory and reasonably explained the transfer pathway of photogenerated charge carriers in the two semiconductors [39]. From then on, a series of S-scheme photocatalytic materials have been reported and successfully applied in the fields of environment and energy [40–47].

Layer-structured molybdenum selenide ( $\text{MoSe}_2$ ) has a narrow band gap (about 1.3–1.9 eV) [48,49], which means it can respond to the whole UV-visible-near-infrared (UV-Vis-NIR) light. However, its multilayer structure and narrow bandgap usually lead to the high recombination rate of photogenerated charge carriers [50]. In this regard, coupling  $\text{MoSe}_2$  with other semiconductors with wide bandgaps is an ideal strategy to take its advantages and simultaneously avoid its flaws. So far, several composite  $\text{MoSe}_2$ -based photocatalysts have been exploited [51–54]. However, to the best of our knowledge, the S-scheme heterojunction photocatalyst based on  $\text{MoSe}_2$  and BiOCl has never been studied.

Herein, we first constructed the S-scheme heterojunction BiOCl/ $\text{MoSe}_2$  photocatalyst by loading  $\text{MoSe}_2$  nanosheets on the surface of BiOCl microcrystals, using a solvothermal method. The morphology and crystalline structures of the as-prepared samples were characterized by the means of scanning electron microscopy (SEM), transmission electron microscopy (TEM), and high-resolution transmission electron microscopy (HR-TEM). The light absorption properties of the samples were analyzed by UV-Vis diffuse reflectance spectroscopy (DRS). The photoelectric properties and the separation rate of charge carriers were investigated using transient photocurrents, electrochemical impedance, and photoluminescent (PL) spectra. The photocatalytic activities of BiOCl and the different BiOCl/ $\text{MoSe}_2$  samples were evaluated by the degradation of azo dye methyl orange (MO) and antibiotic sulfadiazine (SD) under simulated sunlight irradiation. On the basis of the radical trapping experiments and potential analyses of BiOCl and  $\text{MoSe}_2$  conduction bands (CB) and valence bands (VB), the possible photocatalytic mechanism of S-scheme BiOCl/ $\text{MoSe}_2$  was proposed.

## 2. Materials and Methods

### 2.1. Materials

Bismuth nitrate pentahydrate ( $\text{Bi}(\text{NO}_3)_3 \cdot 5\text{H}_2\text{O}$ ) and absolute ethanol ( $\text{C}_2\text{H}_5\text{OH}$ ) were provided by Sinopharm Chemical Reagent Co., Ltd., Shanghai, China. Selenium powder, sodium molybdate dihydrate ( $\text{Na}_2\text{MoO}_4 \cdot 2\text{H}_2\text{O}$ ), and sodium borohydride ( $\text{NaBH}_4$ ) were purchased from Shanghai Adamas Reagent Co., Ltd., Shanghai, China. Potassium chloride (KCl) was obtained from Shanghai Lingfeng Chemical Reagent Co., Ltd., Shanghai, China. All the reagents were analytically pure grade and used as received without further purification. Milli-Q water was homemade and the resistivity was 18.2 M $\Omega$  cm.

## 2.2. Synthesis of BiOCl/MoSe<sub>2</sub>

BiOCl nanosheets were prepared using a hydrothermal method, similar to the previous report [55]. The detailed procedures were as follows: Firstly, 1 mmol Bi(NO<sub>3</sub>)<sub>3</sub>·5H<sub>2</sub>O and 1 mmol KCl were successively dispersed in 15 mL deionized water and stirred at room temperature for 1 h. Then, the mixture was transferred into a 50 mL Teflon-lined stainless-steel autoclave and placed in an oven to react at 160 °C for 24 h. Subsequently, the suspension was cooled to room temperature and the precipitation was washed, respectively, with deionized water and ethanol three times. Finally, the product was dried in a vacuum drying oven at 70 °C for 8 h, denoted as BiOCl.

BiOCl/MoSe<sub>2</sub> was synthesized via a modified solvothermal method [56]: Firstly, 200.5 mg BiOCl, 0.079 mmol Na<sub>2</sub>MoO<sub>4</sub>·2H<sub>2</sub>O, 0.158 mmol selenium powder, and 0.079 mmol NaBH<sub>4</sub> were added into a 25 mL mixture solution of ethanol and water with a volume ratio of 1:1. After the mixture was stirred at room temperature for 1 h, the obtained homogeneous mixture was transferred into a 50 mL Teflon-lined stainless-steel autoclave and kept at 180 °C for 12 h. Then, the autoclave was cooled to room temperature and the obtained precipitate was washed with deionized water and ethanol three times, respectively. Finally, the obtained product was dried in a vacuum drying oven at 70 °C for 8 h. The theoretical loading amount of the MoSe<sub>2</sub> sample was 10 wt.%, denoted as BiOCl/MoSe<sub>2</sub>-10. By changing the dosages of Na<sub>2</sub>MoO<sub>4</sub>·2H<sub>2</sub>O, selenium powder, and NaBH<sub>4</sub>, the BiOCl/MoSe<sub>2</sub> samples with 30 wt.% and 50 wt.% MoSe<sub>2</sub> contents were also synthesized, denoted as BiOCl/MoSe<sub>2</sub>-30 and BiOCl/MoSe<sub>2</sub>-50, respectively. Pure MoSe<sub>2</sub> was further prepared by the same method, except that BiOCl was not added.

## 2.3. Characterization

The morphologies of the obtained samples were observed via scanning electron microscope (SEM, TESCAN VEGA 3 SBH), transmission electron microscope (TEM, JEM2000EX), and high-resolution transmission electron microscope (HR-TEM, JEOL JEM2100). The crystalline structures of the samples were analyzed using a Rigaku D/Max 2550 VB/PC X-ray diffractometer with Cu K $\alpha$  ( $\lambda = 1.5406$  Å) radiation, operated at a voltage of 40 kV and a current of 40 mA. The UV-Vis diffuse reflectance spectra of the samples were recorded on a SHIMADZU UV-2450 spectrophotometer and a Lambda 950 spectrophotometer, equipped with an integrating sphere assembly, using BaSO<sub>4</sub> as the reference material. The photoluminescence (PL) spectra were tested on a Shimadzu RF5301PC fluorescence spectrophotometer and the 320 nm line of Xe lamp was used as the excitation source. The transient photocurrents, electrochemical impedance, and Mott–Schottky spectra were measured by a Zahner electrochemical workstation equipped with a three-electrode system, in which the platinum electrode and saturated calomel electrode were used as the counter electrode and reference electrode, respectively, and 0.2 mg photocatalyst sample was coated on 1.5 cm<sup>2</sup> FTO glass as the working electrode. The transient photocurrent and Mott–Schottky tests were performed in a 0.5 M Na<sub>2</sub>SO<sub>4</sub> aqueous solution and a 300 W Xe lamp with AM 1.5 filter as the light source. A mixed aqueous solution of 2.0 mM K<sub>3</sub>[Fe(CN)<sub>6</sub>], 2.0 mM K<sub>4</sub>[Fe(CN)<sub>6</sub>], and 0.5 M KCl was used as the electrolyte for the electrochemical impedance tests.

## 2.4. Photocatalytic Activity Measurement

The photocatalytic activities of the prepared samples were evaluated by the degradation of methyl orange (MO) and sulfadiazine (SD) under simulated sunlight irradiation, using a 300 W Xe lamp with AM1.5 as the light source. For each measurement, a 50 mg photocatalyst was dispersed in a 50 mL MO/or SD (20 mg/L) solution in a quartz tube and stirred in the dark for 30 min to achieve the adsorption–desorption of MO/or SD on the surface of the photocatalyst. At a given time interval, 5 mL of the mixture solution was withdrawn, centrifuged, and filtered to remove the remaining particles. The residual concentrations of MO and SD were determined using a UV-Vis spectrophotometer and a high-performance liquid chromatograph, respectively.

### 3. Results and Discussion

#### 3.1. Morphological and Crystalline Structures

The morphological structures of the samples were observed by SEM, TEM, and HR-TEM images. As shown in Figure 1A,B, the surface of BiOCl sheets seems to be smooth and the width and thickness of BiOCl sheets are in the range of 1–4.5  $\mu\text{m}$  and 300–400 nm, respectively. From the TEM images of BiOCl and BiOCl/MoSe<sub>2</sub>-30, it can be seen that the block-structured MoSe<sub>2</sub> consists of many thin nanosheets (Figure 1C), which are uniformly wrapped on the surface of BiOCl sheets to form a shell structure (Figure 1D). The lattice structure of BiOCl/MoSe<sub>2</sub>-30 was further analyzed using HR-TEM images. In Figure 1E, the lattice spacing was measured to be 0.65 nm, attributed to the (0 0 2) crystal planes of 2H phase MoSe<sub>2</sub> [57]. In Figure 1F, the lattice spacing of 0.275 nm corresponds to BiOCl (1 1 0) crystal planes, while that of 0.28 nm is attributed to MoSe<sub>2</sub> (1 0 0) crystal planes. These results demonstrate the formation of a BiOCl/MoSe<sub>2</sub> heterojunction structure [58].

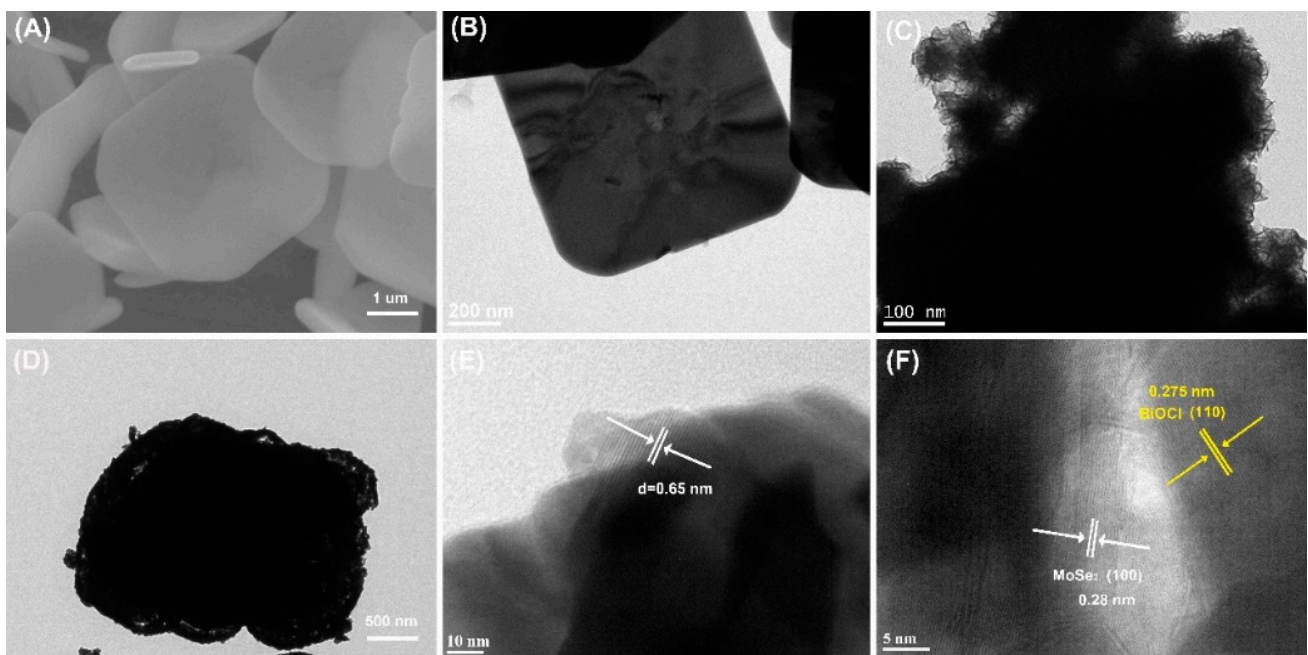


**Figure 1.** (A) SEM image of BiOCl. (B–D) TEM images of (B) BiOCl, (C) MoSe<sub>2</sub>, and (D) BiOCl/MoSe<sub>2</sub>-30. (E,F) HR-TEM images of BiOCl/MoSe<sub>2</sub>-30.

The crystalline structures of the synthesized samples were analyzed by X-ray diffraction patterns (XRD). As shown in Figure 2, BiOCl presents the diffraction peaks at  $2\theta = 24.1^\circ, 25.9^\circ, 33.4^\circ, 36.5^\circ, 40.9^\circ, 49.7^\circ, 54.1^\circ, 63.1^\circ,$  and  $68.1^\circ$ , attributed to BiOCl (0 0 2), (1 0 1), (1 0 2), (0 0 3), (1 1 2), (1 1 3), (2 1 1), (2 0 3), and (2 2 0) crystal planes, respectively (JCPDS No. 06-0249) [54]. In contrast, BiOCl/MoSe<sub>2</sub>-10, BiOCl/MoSe<sub>2</sub>-30, and BiOCl/MoSe<sub>2</sub>-50 exhibit an obvious diffraction peak at  $24.1^\circ$ , while the other characteristic peaks become very weak, due to the resistance of the thick MoSe<sub>2</sub> shell layer to X-ray. Even enlarged 10 times in intensity, the diffraction peaks of MoSe<sub>2</sub> (1 0 2) and (1 1 0) are still very weak and broad, which is probably ascribable to both its low crystallinity as well as the very thin sheet structure.

#### 3.2. Light Absorption and PL Properties

The optical properties of MoSe<sub>2</sub>, BiOCl, and BiOCl/MoSe<sub>2</sub> were investigated by UV-Vis DRS and PL spectra. As shown in Figure 3A,B, pure BiOCl only can absorb UV light, while MoSe<sub>2</sub> displays strong light absorption in the whole UV-Vis-NIR region. After coupling with MoSe<sub>2</sub>, all the BiOCl/MoSe<sub>2</sub> samples exhibit a significantly enhanced absorption in the visible and NIR region, and the absorption intensity gradually increases



with the increase of MoSe<sub>2</sub> content. PL spectrum is a useful technique to investigate the trapping, migration, and transfer efficiency of the photogenerated charge carriers in semiconductor photocatalysts [31,59,60]. Herein, we tested the PL spectra of BiOCl and the different BiOCl/MoSe<sub>2</sub> samples at room temperature with an excitation wavelength of 320 nm. As displayed in Figure 3C, BiOCl exhibits a strong PL emission band in the range of 350–550 nm, while all the BiOCl/MoSe<sub>2</sub> samples only have a very weak PL emission peak at 470 nm. After increasing the luminous flux of excitation light, the three BiOCl/MoSe<sub>2</sub> samples also exhibit the PL emission bands in the range of 350–550 nm, similar to that of BiOCl (Figure 3D). The PL intensity of BiOCl/MoSe<sub>2</sub>-30 is near to that of BiOCl/MoSe<sub>2</sub>-50 and obviously weaker than that of BiOCl/MoSe<sub>2</sub>-10. These results indicate that the coupling of BiOCl and MoSe<sub>2</sub> can effectively restrain the recombination of photogenerated charge carriers and that 30 wt.% is the optimal MoSe<sub>2</sub> loading amount for effectively separating the photogenerated electrons and holes.

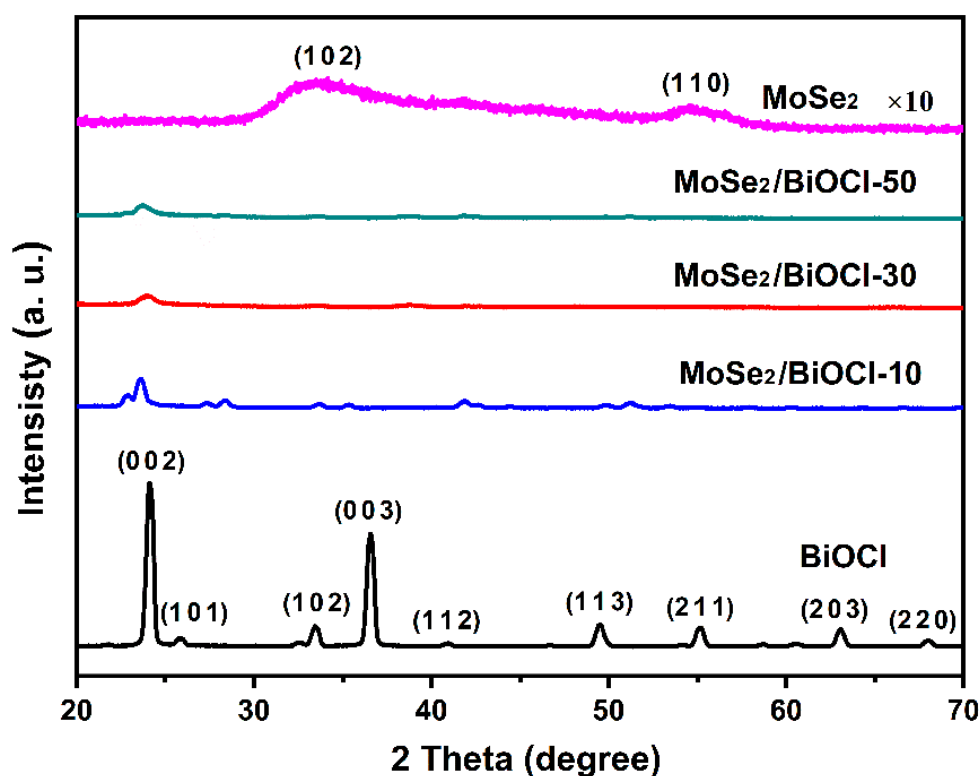
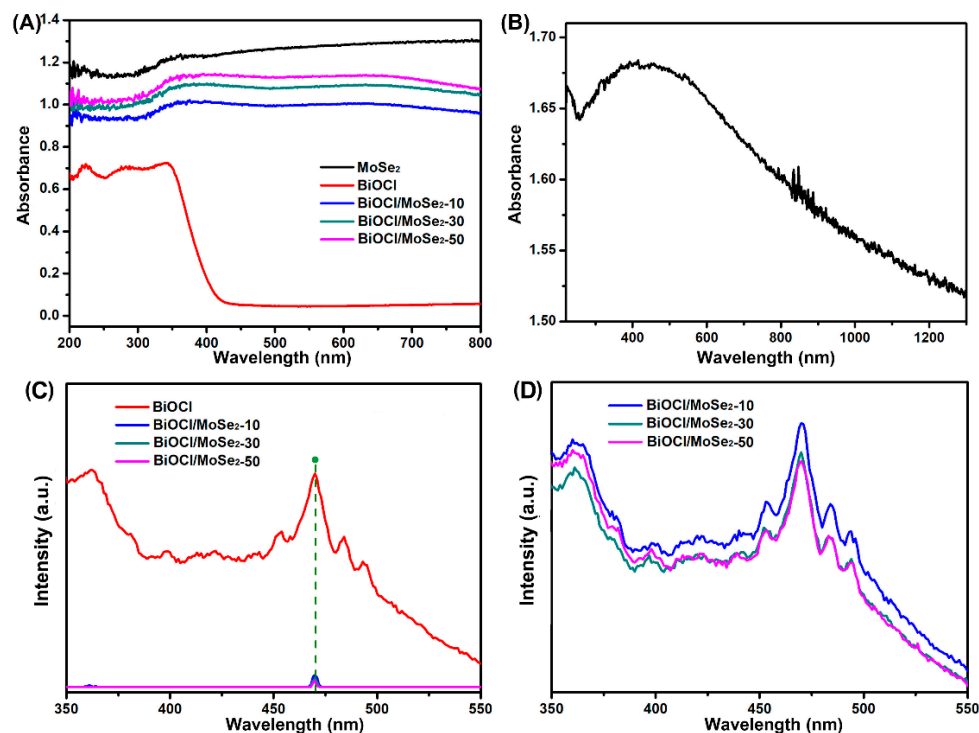


Figure 2. XRD patterns of MoSe<sub>2</sub>, BiOCl, BiOCl/MoSe<sub>2</sub>-10, BiOCl/MoSe<sub>2</sub>-30, and BiOCl/MoSe<sub>2</sub>-50.

### 3.3. Photoelectric Characteristics

The photoelectric characteristics of BiOCl and the different BiOCl/MoSe<sub>2</sub> samples were investigated by transient photocurrent measurements, which can further disclose the production, separation, and transfer efficiency of photogenerated charge carriers in these samples. As shown in Figure 4A, both BiOCl and MoSe<sub>2</sub> exhibit very weak photocurrent intensity due to the low sunlight response ability and the high recombination rate of photo-generated electrons and holes, respectively. In contrast, all the BiOCl/MoSe<sub>2</sub> composite photocatalysts display obviously enhanced current photocurrent intensity, indicating that the formation of a heterojunction structure can effectively promote the separation and transfer of photogenerated charge carriers. Amongst these samples, BiOCl/MoSe<sub>2</sub>-30 shows the highest photocurrent intensity, which is about four times that of pure BiOCl. For BiOCl/MoSe<sub>2</sub>-50, its photocurrent intensity is evidently weaker than that of BiOCl/MoSe<sub>2</sub>-30, resulting from the shielding of excess MoSe<sub>2</sub> to light [61]. The electrochemical impedance spectra (EIS) can be used to disclose the dynamics of the mobile and bound charges in the interfacial or bulk regions of semiconductors, and the smaller

curvature radius usually implies the weaker resistance to charge transfer [14,62,63]. In the EIS Nyquist spectra of Figure 4B, all the BiOCl/MoSe<sub>2</sub> samples exhibit much smaller semicircle diameters than BiOCl, implying that coupling MoSe<sub>2</sub> can effectively decrease the transfer resistance of the carriers in BiOCl. As the loading amount of MoSe<sub>2</sub> increases from 10 wt.% to 30 wt.%, the semicircle diameter of the EIS curve obviously becomes smaller and it almost has no change when the loading amount of MoSe<sub>2</sub> is further increased to 30 wt.%. Combining the results of the transient photocurrents and EIS spectra, it can be concluded that 30 wt.% is the optimal MoSe<sub>2</sub> loading amount for effectively facilitating the production, separation, and transfer of photogenerated charge carriers.



**Figure 3.** (A) UV–Vis DRS spectra of MoSe<sub>2</sub>, BiOCl, BiOCl/MoSe<sub>2</sub>-10, BiOCl/MoSe<sub>2</sub>-30, and BiOCl/MoSe<sub>2</sub>-50 in the UV and visible light region. (B) DRS spectra of MoSe<sub>2</sub> in the UV, visible light, and NIR region. (C) PL spectra of BiOCl, BiOCl/MoSe<sub>2</sub>-10, BiOCl/MoSe<sub>2</sub>-30, and BiOCl/MoSe<sub>2</sub>-50. (D) Enhanced PL spectra of BiOCl/MoSe<sub>2</sub>-10, BiOCl/MoSe<sub>2</sub>-30, and BiOCl/MoSe<sub>2</sub>-50.

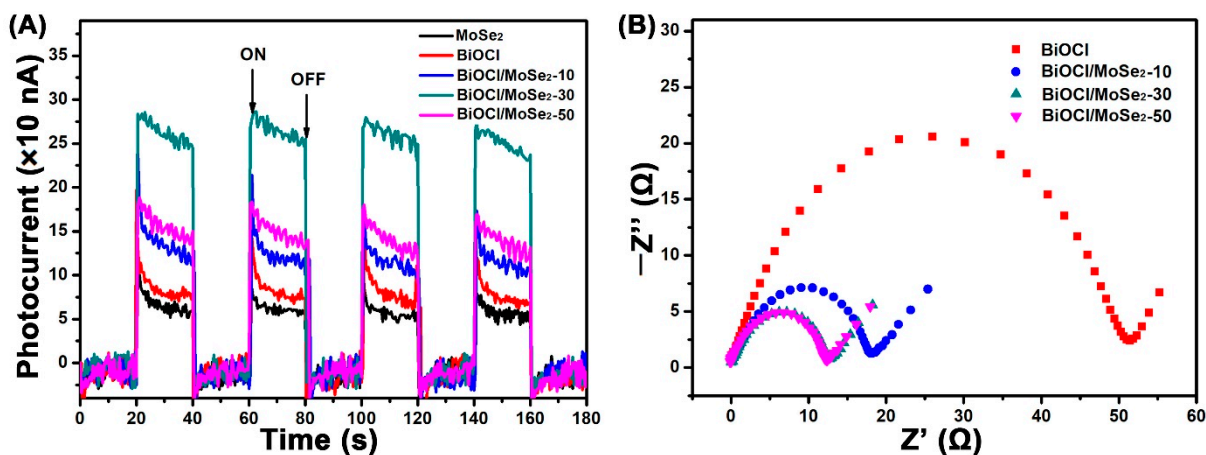


**Figure 4.** (A) Transient photocurrents of MoSe<sub>2</sub>, BiOCl, BiOCl/MoSe<sub>2</sub>-10, BiOCl/MoSe<sub>2</sub>-30, and BiOCl/MoSe<sub>2</sub>-50 under simulated sunlight irradiation; (B) Nyquist plots of the electrochemical impedance spectra of BiOCl, BiOCl/MoSe<sub>2</sub>-10, BiOCl/MoSe<sub>2</sub>-30, and BiOCl/MoSe<sub>2</sub>-50.

### 3.4. Photocatalytic Activity and Mechanism

Figure 5A,B presents the degradation curves of MO and SD over the different photocatalysts under simulated sunlight irradiation, respectively. In the absence of photocatalyst, the concentrations of MO and SD almost have no change under simulated sunlight irradiation, indicating that they have high photostability. Both pure BiOCl and MoSe<sub>2</sub> exhibit low photocatalytic activity for MO and SD degradation, which is because BiOCl cannot respond to visible light while MoSe<sub>2</sub> has the high recombination rate of photogenerated electrons and holes. Compared to pure MoSe<sub>2</sub> and BiOCl, all the BiOCl/MoSe<sub>2</sub> samples show evidently enhanced photocatalytic activity for MO and SD degradation, because the heterojunction structure between MoSe<sub>2</sub> and BiOCl can effectively restrain the recombination of photogenerated electrons and holes. To more accurately compare the photocatalytic activities of BiOCl and the different BiOCl/MoSe<sub>2</sub> samples, we further fitted the kinetic curves of MO and SD degradations over these samples. From Figure 5C,D, it can be seen that the degradations of MO and SD over these photocatalysts follow the pseudo first-order kinetic reaction. By comparing the reaction kinetic constants in Table 1, we know that BiOCl/MoSe<sub>2</sub>-30 possesses the highest photocatalytic activity among all the samples.

**Table 1.** The kinetic constants of photocatalytic degradation of MO and SD over the different samples.

Sample	MoSe <sub>2</sub>	BiOCl	BiOCl/MoSe <sub>2</sub> -10	BiOCl/MoSe <sub>2</sub> -30	BiOCl/MoSe <sub>2</sub> -50
MO (min <sup>-1</sup> )	0.0020	0.0027	0.0063	0.0307	0.0082
SD (h <sup>-1</sup> )	0.1246	0.3258	0.5829	0.9323	0.4004

Given that photostability is very important to a photocatalyst for its practical applications, we further tested the photostability of BiOCl/MoSe<sub>2</sub>-30 using the cyclic degradation experiments of MO and SD under simulated sunlight irradiation. As shown in Figure 5E, the degradation rates of MO and SD only display a slight decrease after four cycles, probably due to the inevitable loss of photocatalysts during the recycle runs. This result indicates that BiOCl/MoSe<sub>2</sub>-30 is a stable photocatalyst under simulated sunlight irradiation. In the photocatalytic degradation process, the reactive species that take part in the organic pollutant decomposition mainly include hydroxyl radical (•OH), superoxide radical (•O<sub>2</sub><sup>-</sup>), and hole (h<sup>+</sup>). Herein, we identified the produced reactive species over BiOCl/MoSe<sub>2</sub>-30 in the organic decomposition process by addition of radical trapping agents. It is known that •OH, h<sup>+</sup>, and •O<sub>2</sub><sup>-</sup> can be quenched by tert-butanol (TBA), EDTA-2Na, and p-benzoquinone (PBQ), respectively. As shown in Figure 5F, the degradation rate of MO was evidently inhibited after addition of EDTA-2Na, PBQ, and TBA, implying that all h<sup>+</sup>, •O<sub>2</sub><sup>-</sup>, and •OH take part in the degradation of MO. The effect of these species for MO degradation decreases in the order of h<sup>+</sup> > •O<sub>2</sub><sup>-</sup> > •OH.

To clarify the migration pathways of photogenerated charge carriers in BiOCl/MoSe<sub>2</sub>, it is necessary to identify the conduction band (CB) and valence band (VB) potentials of MoSe<sub>2</sub> and BiOCl. In our previous studies [14,62], we have calculated the potentials of BiOCl CB and VB, which are +0.14 eV and +3.51 eV, respectively. Herein, we estimated the potentials of MoSe<sub>2</sub> CB and VB by analyzing its UV-Vis absorption spectrum and Mott–Schottky curve.

Firstly, the bandgap energy of MoSe<sub>2</sub> nanosheets was calculated using Tauc plot via the following Kubelka–Munk equation [64]:

$$(\alpha h\nu)^2 = A(h\nu - E_g) \quad (1)$$

where  $h$ ,  $\alpha$ ,  $\nu$ ,  $A$ , and  $E_g$  are the Planck constant, absorption coefficient, light frequency, constant value, and bandgap energy, respectively. As shown in Figure 6A, the bandgap energy of MoSe<sub>2</sub> was estimated to be 1.9 eV, similar to the value of the previous reports [52,65,66]. Then, the potential of MoSe<sub>2</sub> CB edge was determined by Mott–Schottky analysis [67]. As shown in Figure 6B, the potential of MoSe<sub>2</sub> CB ( $E_{CB}$ ) was estimated using the extrapolation of the Mott–Schottky plots at different frequencies (1 kHz, 2 kHz, and 3 kHz) to be  $-0.59$  V

(vs. NHE). According to the equation of  $E_{VB} = E_{CB} + E_g$  ( $E_{VB}$  is the potential of VB), the potential of MoSe<sub>2</sub> VB was further calculated to be 1.31 eV.

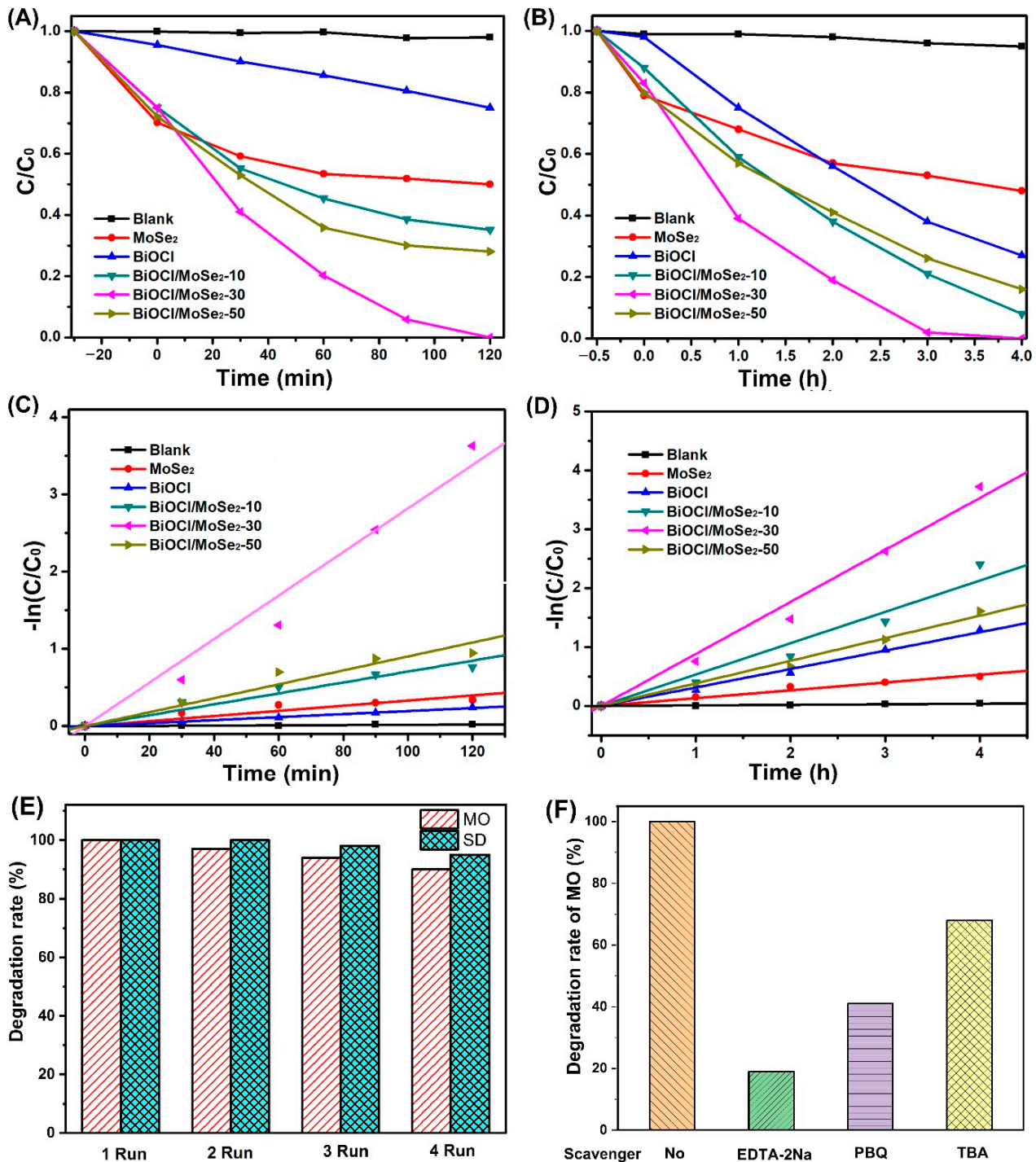


**Figure 5.** (A,B) Photocatalytic degradation curves of (A) MO and (B) SD over the different photocatalysts under simulated sunlight irradiation. Corresponding fitted degradation kinetic curves of (C) MO and (D) SD. (E) Cyclic photocatalytic degradations of MO and SD over BiOCl/MoSe<sub>2</sub>-30. The reaction time of each cycle experiment for MO is 120 min and that for SD is 4 h. (F) Photocatalytic degradation rates of MO over BiOCl/MoSe<sub>2</sub>-30 in the presence of different radical scavengers.



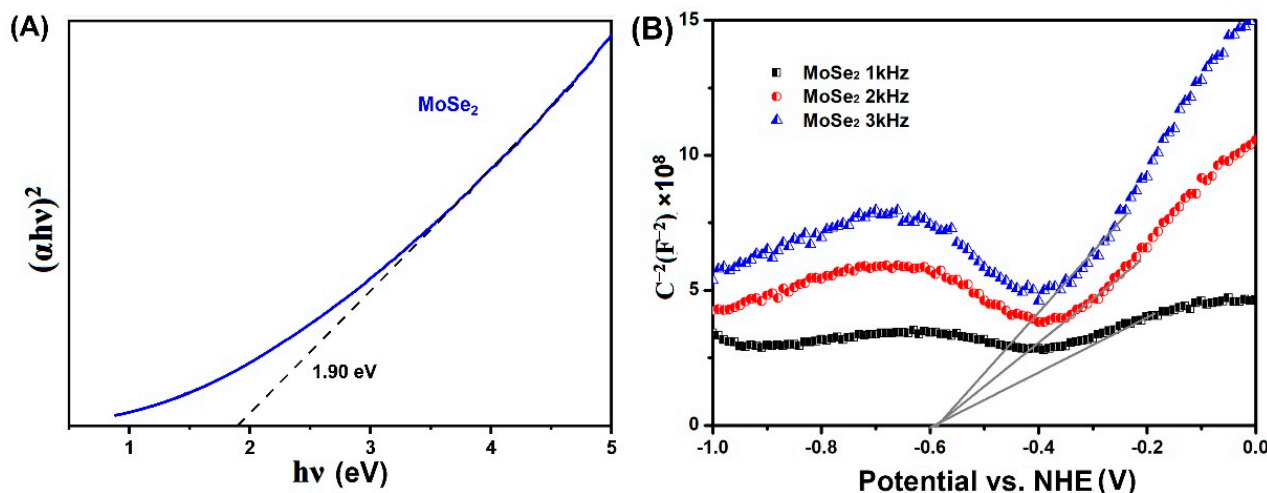


Figure 6. (A) Plots of  $(\alpha hv)^2$  (MoSe<sub>2</sub>) versus photon energy ( $h\nu$ ); (B) Mott-Schottky plots of MoSe<sub>2</sub>.

On the basis of the CB and VB potentials of BiOCl and MoSe<sub>2</sub>, BiOCl/MoSe<sub>2</sub> should be ascribed to one of the three types of heterojunction, i.e., Type-II, direct Z-scheme, and S-scheme. Firstly, assuming that BiOCl/MoSe<sub>2</sub> is a Type-II semiconductor, the electrons on MoSe<sub>2</sub> CB would migrate to BiOCl CB. Given that the potential of BiOCl CB (0.14 eV vs. NHE) is more positive than  $E_0(\text{O}_2/\bullet\text{O}_2^-)$  (−0.33 eV vs. MHE) [68–70], the adsorbed O<sub>2</sub> cannot be reduced by the electrons on BiOCl CB to form  $\bullet\text{O}_2^-$ . Similarly, since the potential of MoSe<sub>2</sub> VB (1.31 eV vs. NHE) is more negative than  $E_0(\bullet\text{OH}/\text{OH}^-)$  (1.99 eV vs. NHE) [68–70], the holes on MoSe<sub>2</sub> VB cannot oxidize OH<sup>−</sup> into  $\bullet\text{OH}$ . However, the presence of  $\bullet\text{O}_2^-$  and  $\bullet\text{OH}$  has been proved by the radical trapping experiments (Figure 5F), implying that BiOCl/MoSe<sub>2</sub> is not a traditional Type-II semiconductor and the electrons for  $\bullet\text{O}_2^-$  production and the holes for  $\bullet\text{OH}$  production come from the MoSe<sub>2</sub> CB and BiOCl VB, respectively. Moreover, Z-scheme heterojunction also has a theoretical problem in explaining the transfer pathway of photogenerated electrons and holes in BiOCl/MoSe<sub>2</sub>: from the perspective of charge transfer, the electrons on MoSe<sub>2</sub> CB will preferentially recombine with the holes on BiOCl VB, rather than the electrons on BiOCl CB recombine with the holes on MoSe<sub>2</sub> VB.

The S-scheme heterojunction is more reasonable to illustrate the transfer pathway of photogenerated electrons and holes in BiOCl/MoSe<sub>2</sub> [39,41,71,72]—in this composite photocatalytic system, BiOCl is the oxidation photocatalyst (OP) and MoSe<sub>2</sub> is the reduction photocatalyst (RP), both of which form an S-scheme heterojunction [39,41,71,72]. After the two components are in close contact, the electrons in MoSe<sub>2</sub> spontaneously transfer to BiOCl, producing an electron depletion layer and electron accumulation layer near the interface of MoSe<sub>2</sub> and BiOCl, respectively. Thus, MoSe<sub>2</sub> would be positively charged and BiOCl would be negatively charged, forming an internal electric field directing from MoSe<sub>2</sub> to BiOCl. Meanwhile, after BiOCl and MoSe<sub>2</sub> contact together, their Fermi energy should be aligned to the same level. Thus, the Fermi levels of BiOCl and MoSe<sub>2</sub> should upward shift and downward shift, respectively, together with the band bending at their interfaces. Both the coulomb force of electric field and the band bending urge the photogenerated electrons from BiOCl to recombine with the holes from MoSe<sub>2</sub> VB. Due to the band bending, the electrons on MoSe<sub>2</sub> CB and holes on BiOCl will be reserved.

Based on the above experimental results and analyses, the degradation mechanism of organic pollutants over S-scheme BiOCl/MoSe<sub>2</sub> was proposed: As illustrated in Figure 7, under simulated sunlight irradiation, both BiOCl and MoSe<sub>2</sub> can produce holes on their VB and electrons on their CB. Using the acceleration of internal electric field, the photogenerated electrons on BiOCl CB and the holes on MoSe<sub>2</sub> would be recombined. As a result, the powerful electrons on MoSe<sub>2</sub> CB and the powerful holes on BiOCl VB would be reserved. Subsequently, the electrons on MoSe<sub>2</sub> CB would react with adsorbed O<sub>2</sub> to form  $\bullet\text{O}_2^-$ .

Meanwhile, some holes on the BiOCl VB would oxidize  $\text{OH}^-$  to produce  $\bullet\text{OH}$ . All of  $\bullet\text{O}_2^-$ ,  $\bullet\text{OH}$ , and  $\text{h}^+$  take part in the degradation of organic pollutants.

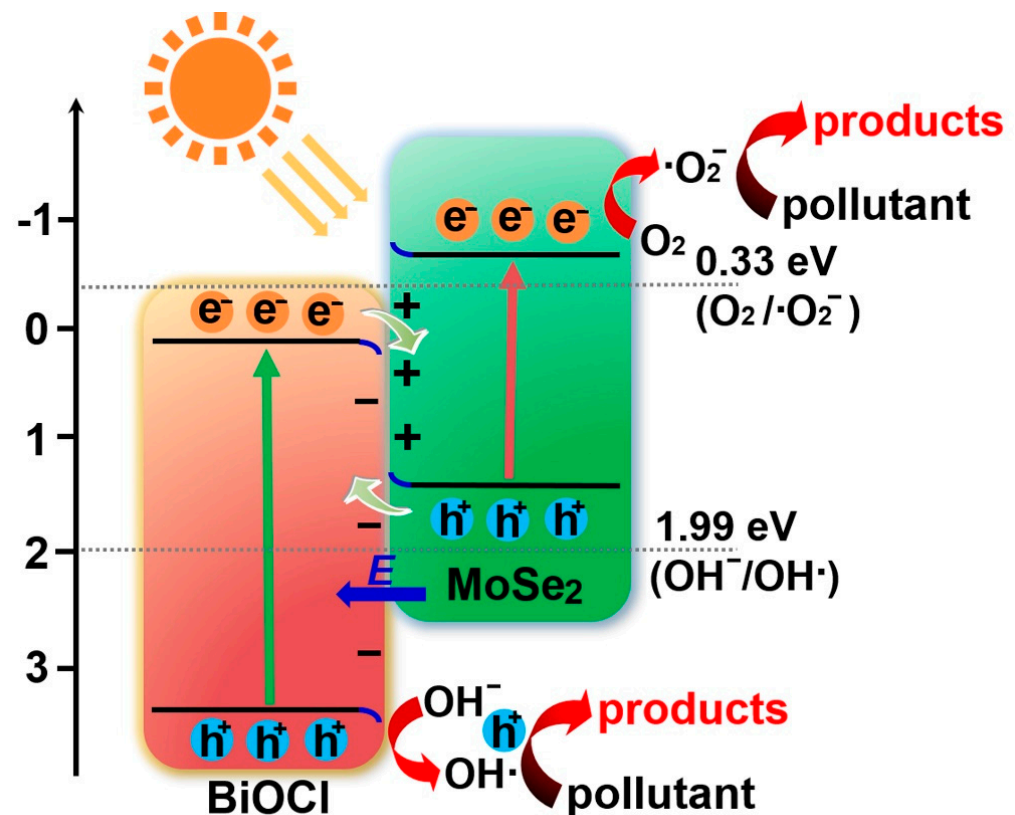


Figure 7. Proposed photocatalytic mechanism of S-scheme BiOCl/MoSe<sub>2</sub>.

#### 4. Conclusions

In summary, S-scheme BiOCl/MoSe<sub>2</sub> heterojunction was fabricated via a modified solvothermal method. It was found that the thin MoSe<sub>2</sub> nanosheets are uniformly wrapped on the surface of BiOCl microcrystals to form a shell structure. The MoSe<sub>2</sub> diffraction peaks of MoSe<sub>2</sub> and the different BiOCl/MoSe<sub>2</sub> samples are very weak due to its low crystallinity and thin layer structure. The UV-Vis diffuse reflectance spectra show that all the BiOCl/MoSe<sub>2</sub> samples exhibit a significantly enhanced absorption in the visible and near-infrared light region when compared with BiOCl, and the absorption intensity gradually increases with the increase of MoSe<sub>2</sub> content. From the photoluminescence spectra, transient photocurrents, and electrochemical impedance spectra, it can be concluded that the BiOCl/MoSe<sub>2</sub> heterojunction can effectively promote the transfer of photogenerated charge carriers. The results of MO and SD degradations indicate that all the BiOCl/MoSe<sub>2</sub> samples display an evidently enhanced photocatalytic activity compared to single BiOCl and MoSe<sub>2</sub>, and the optimal MoSe<sub>2</sub> loading amount for obtaining the highest photocatalytic activity is 30 wt.%. The radical trapping experiments disclosed that all  $\text{h}^+$ ,  $\bullet\text{O}_2^-$ , and  $\bullet\text{OH}$  take part in the degradation of organic pollutants and  $\text{h}^+$  plays a more important role than  $\bullet\text{O}_2^-$  and  $\bullet\text{OH}$ . By further analyzing the potentials of BiOCl and MoSe<sub>2</sub> CB and VB, it can be deduced that the BiOCl/MoSe<sub>2</sub> follows an S-scheme photocatalytic mechanism. We think that this study provides a reference for fabricating the S-scheme photocatalytic materials to eliminate the organic pollutants in wastewater under sunlight irradiation.

**Author Contributions:** Conceptualization, B.T., J.Z. and Z.G.; methodology, Y.H., F.C. and Z.G.; formal analysis, Y.H. and Z.G.; Investigation, Y.L. (Yusheng Luo); data curation, F.C.; writing—original draft preparation, Y.H.; writing—review and editing, B.T.; visualization, L.Z. and Y.L. (Yufeng Lu); supervision, B.T. and J.Z. All authors have read and agreed to the published version of the manuscript.

**Funding:** This research was funded by the National Natural Science Foundation of China (U1862112 and 21573069), Shanghai Municipal Science and Technology Major Project (2018SHZDZX03), Program of Introducing Talents of Discipline to Universities (B16017), Fundamental Research Funds for the Central Universities (50321041917001 and 50321042017001), and Fundamental Research Funds for the Central Universities (JKD01211701).

**Institutional Review Board Statement:** Not applicable.

**Informed Consent Statement:** Not applicable.

**Acknowledgments:** All authors gratefully acknowledge the support of Science and Technology on Particle Transport and Separation Laboratory.

**Conflicts of Interest:** The authors declare no conflict of interest.

## References

1. Som, I.; Roy, M.; Saha, R. Advances in nanomaterial-based water treatment approaches for photocatalytic degradation of water pollutants. *ChemCatChem* **2020**, *12*, 3409–3433. [[CrossRef](#)]
2. Ren, G.M.; Han, H.T.; Wang, Y.X.; Liu, S.T.; Zhao, J.Y.; Meng, X.C.; Li, Z.Z. Recent advances of photocatalytic application in watertreatment: A review. *Nanomaterials* **2021**, *11*, 1804. [[CrossRef](#)] [[PubMed](#)]
3. Natarajan, S.; Bajaj, H.C.; Tayade, R.J. Recent advances based on the synergetic effect of adsorption for removal of dyes from waste water using photocatalytic process. *J. Environ. Sci.* **2018**, *65*, 201–222. [[CrossRef](#)] [[PubMed](#)]
4. Molinari, R.; Pirillo, F.; Loddo, V.; Palmisano, L. Heterogeneous photocatalytic degradation of pharmaceuticals in water by using polycrystalline TiO<sub>2</sub> and a nanofiltration membrane reactor. *Catal. Today* **2006**, *118*, 205–213. [[CrossRef](#)]
5. Mendez-Arriaga, F.; Esplugas, S.; Giménez, J. Photocatalytic degradation of non-steroidal anti-inflammatory drugs with TiO<sub>2</sub> and simulated solar irradiation. *Water Res.* **2008**, *42*, 585–594. [[CrossRef](#)]
6. Hu, J.L.; Yang, Q.H.; Lin, H.; Ye, Y.P.; He, Q.; Zhang, J.N.; Qian, H.S. Mesoporous silica nanospheres decorated with CdS nanocrystals for enhanced photocatalytic and excellent antibacterial activities. *Nanoscale* **2013**, *5*, 6327–6332. [[CrossRef](#)]
7. Dong, R.F.; Tian, B.Z.; Zhang, J.L.; Wang, T.T.; Tao, Q.S.; Bao, S.Y.; Yang, F.; Zeng, C.Y. AgBr@Ag/TiO<sub>2</sub> core-shell composite with excellent visible light photocatalytic activity and hydrothermal stability. *Catal. Commun.* **2013**, *38*, 16–20. [[CrossRef](#)]
8. Elmolla, E.S.; Chaudhuri, M. Photocatalytic degradation of amoxicillin, ampicillin and cloxacillin antibiotics in aqueous solution using UV/TiO<sub>2</sub> and UV/H<sub>2</sub>O<sub>2</sub>/TiO<sub>2</sub> photocatalysis. *Desalination* **2010**, *252*, 46–52. [[CrossRef](#)]
9. Sarayu, K.; Sandhya, S. Current technologies for biological treatment of textile wastewater—A review. *Appl. Biochem. Biotechnol.* **2012**, *167*, 645–661. [[CrossRef](#)]
10. Palominos, R.A.; Mondaca, M.A.; Giraldo, A.; Peñuela, G.; Perez-Moya, M.; Mansilla, H.D. Photocatalytic oxidation of the antibiotic tetracycline on TiO<sub>2</sub> and ZnO suspensions. *Catal. Today* **2009**, *144*, 100–105. [[CrossRef](#)]
11. Wang, P.H.; Yap, P.S.; Lim, T.T. C–N–S tridoped TiO<sub>2</sub> for photocatalytic degradation of tetracycline under visible-light irradiation. *Appl. Catal. A* **2011**, *399*, 252–261. [[CrossRef](#)]
12. Crini, G.; Lichtfouse, E. Advantages and disadvantages of techniques used for wastewater treatment. *Environ. Chem. Lett.* **2019**, *17*, 145–155. [[CrossRef](#)]
13. Bao, S.Y.; Wu, Q.F.; Chang, S.Z.; Tian, B.Z.; Zhang, J.L. Z-scheme CdS–Au–BiVO<sub>4</sub> with enhanced photocatalytic activity for organic contaminant decomposition. *Catal. Sci. Technol.* **2017**, *7*, 124–132. [[CrossRef](#)]
14. Li, Q.Y.; Guan, Z.P.; Wu, D.; Zhao, X.G.; Bao, S.Y.; Tian, B.Z.; Zhang, J.L. Z-scheme BiOCl–Au–CdS heterostructure with enhanced sunlight-driven photocatalytic activity in degrading water dyes and antibiotics. *ACS Sustain. Chem. Eng.* **2017**, *5*, 6958–6968. [[CrossRef](#)]
15. Kong, W.H.; Wang, S.L.; Wu, D.; Chen, C.R.; Luo, Y.S.; Pei, Y.T.; Tian, B.Z.; Zhang, J.L. Fabrication of 3D sponge@AgBr–AgCl/Ag and tubular photoreactor for continuous wastewater purification under sunlight irradiation. *ACS Sustain. Chem. Eng.* **2019**, *7*, 14051–14063. [[CrossRef](#)]
16. Cheng, T.T.; Gao, H.J.; Liu, G.R.; Pu, Z.S.; Wang, S.F.; Yi, Z.; Wu, X.W.; Yang, H. Preparation of core-shell heterojunction photocatalysts by coating CdS nanoparticles onto Bi<sub>4</sub>Ti<sub>3</sub>O<sub>12</sub> hierarchical microspheres and their photocatalytic removal of organic pollutants and Cr(VI) ions. *Colloid Surf. A* **2022**, *633*, 127918. [[CrossRef](#)]
17. Li, L.X.; Gao, H.J.; Yi, Z.; Wang, S.F.; Wu, X.W.; Li, R.S.; Yang, H. Comparative investigation on synthesis, morphological tailoring and photocatalytic activities of Bi<sub>2</sub>O<sub>2</sub>CO<sub>3</sub> nanostructures. *Colloid Surf. A* **2022**, *644*, 128758. [[CrossRef](#)]
18. Chen, H.; Chen, Z.H.; Yang, H.; Wen, L.H.; Yi, Z.; Zhou, Z.G.; Dai, B.; Zhang, J.G.; Wu, X.W.; Wu, P.H. Multi-mode surface plasmon resonance absorber based on dart-type single-layer graphene. *RSC Adv.* **2022**, *12*, 7821–7829. [[CrossRef](#)]

19. Li, L.X.; Sun, X.F.; Xian, T.; Gao, H.J.; Wang, S.F.; Yi, Z.; Wu, X.W.; Yang, H. Template-free synthesis of Bi<sub>2</sub>O<sub>2</sub>CO<sub>3</sub> hierarchical nanotubes self-assembled from ordered nanoplates for promising photocatalytic application. *Phys. Chem. Chem. Phys.* **2022**, *24*, 8279–8295. [[CrossRef](#)]
20. Lei, Y.Q.; Wang, G.H.; Song, S.Y.; Fan, W.Q.; Zhang, H.J. Synthesis, characterization and assembly of BiOCl nanostructure and their photocatalytic properties. *CrystEngComm* **2009**, *11*, 1857–1862. [[CrossRef](#)]
21. Zhang, X.; Ai, Z.H.; Jia, F.L.; Zhang, L.Z. Generalized one-pot synthesis, characterization, and photocatalytic activity of hierarchical BiOX (X = Cl, Br, I) nanoplate microspheres. *J. Phys. Chem. C* **2008**, *112*, 747–753. [[CrossRef](#)]
22. Guan, M.L.; Xiao, C.; Zhang, J.; Fan, S.J.; An, R.; Cheng, Q.M.; Xie, J.F.; Zhou, M.; Ye, B.J.; Xie, Y. Vacancy associates promoting solar-driven photocatalytic activity of ultrathin bismuth oxychloride nanosheets. *J. Am. Chem. Soc.* **2013**, *135*, 10411–10417. [[CrossRef](#)] [[PubMed](#)]
23. Zhao, K.; Zhang, L.Z.; Wang, J.J.; Li, Q.X.; He, W.W.; Yin, J.J. Surface structure-dependent molecular oxygen activation of BiOCl single-crystalline nanosheets. *J. Am. Chem. Soc.* **2013**, *135*, 15750–15753. [[CrossRef](#)] [[PubMed](#)]
24. Ye, L.Q.; Deng, K.J.; Xu, F.; Tian, L.H.; Peng, T.Y.; Zan, L. Increasing visible-light absorption for photocatalysis with black BiOCl. *Phys. Chem. Chem. Phys.* **2012**, *14*, 82–85. [[CrossRef](#)] [[PubMed](#)]
25. Weng, S.X.; Chen, B.B.; Xie, L.Y.; Zheng, Z.Y.; Liu, P. Facile in situ synthesis of a Bi/BiOCl nanocomposite with high photocatalytic activity. *J. Mater. Chem. A* **2013**, *1*, 3068–3075. [[CrossRef](#)]
26. Dong, F.; Xiong, T.; Yan, S.; Wang, H.Q.; Sun, Y.J.; Zhang, Y.X.; Huang, H.W.; Wu, Z.B. Facets and defects cooperatively promote visible light plasmonic photocatalysis with Bi nanowires@BiOCl nanosheets. *J. Catal.* **2016**, *344*, 401–410. [[CrossRef](#)]
27. Jiang, J.; Zhang, L.Z.; Li, H.; He, W.W.; Yin, J.J. Self-doping and surface plasmon modification induced visible light photocatalysis of BiOCl. *Nanoscale* **2013**, *5*, 10573–10581. [[CrossRef](#)]
28. Tan, C.W.; Zhu, G.Q.; Hojamberdiev, M.; Okada, K.; Liang, J.C.; Luo, X.; Liu, P.; Liu, Y. Co<sub>3</sub>O<sub>4</sub> nanoparticles-loaded BiOCl nanoplates with the dominant {001} facets: Efficient photodegradation of organic dyes under visible light. *Appl. Catal. B* **2014**, *152–153*, 425–436. [[CrossRef](#)]
29. Li, T.B.; Chen, G.; Zhou, C.; Shen, Z.Y.; Jin, R.C.; Sun, J.X. New photocatalyst BiOCl/BiOI composites with highly enhanced visible light photocatalytic performances. *Dalton Trans.* **2011**, *40*, 6751–6758. [[CrossRef](#)]
30. Yu, L.H.; Zhang, X.Y.; Li, G.W.; Cao, Y.T.; Shao, Y.; Li, D.Z. Highly efficient Bi<sub>2</sub>O<sub>2</sub>CO<sub>3</sub>/BiOCl photocatalyst based on heterojunction with enhanced dye-sensitization. *Appl. Catal. B* **2016**, *187*, 301–309. [[CrossRef](#)]
31. Bao, S.Y.; Wang, Z.; Zhang, J.L.; Tian, B.Z. Facet-heterojunction-based Z-Scheme BiVO<sub>4</sub>{010} microplates decorated with AgBr-Ag nanoparticles for the photocatalytic inactivation of bacteria and the decomposition of organic contaminants. *ACS Appl. Nano Mater.* **2020**, *3*, 8604–8617. [[CrossRef](#)]
32. Yuan, Z.; Huang, H.; Li, N.; Chen, D.; Xu, Q.; Li, H.; He, J.; Lu, J. All-solid-state WO<sub>3</sub>/TQDs/In<sub>2</sub>S<sub>3</sub> Z-scheme heterojunctions bridged by Ti<sub>3</sub>C<sub>2</sub> quantum dots for efficient removal of hexavalent chromium and bisphenol A. *J. Hazard. Mater.* **2021**, *409*, 125027. [[CrossRef](#)] [[PubMed](#)]
33. Wen, X.J.; Niu, C.G.; Zhang, L.; Liang, C.; Guo, H.; Zeng, G.M. Photocatalytic degradation of ciprofloxacin by a novel Z-scheme CeO<sub>2</sub>-Ag/AgBr photocatalyst: Influencing factors, possible degradation pathways, and mechanism insight. *J. Catal.* **2018**, *358*, 141–154. [[CrossRef](#)]
34. Jo, W.K.; Natarajan, T.S. Influence of TiO<sub>2</sub> morphology on the photocatalytic efficiency of direct Z-scheme g-C<sub>3</sub>N<sub>4</sub>/TiO<sub>2</sub> photocatalysts for isoniazid degradation. *Chem. Eng. J.* **2015**, *281*, 549–565. [[CrossRef](#)]
35. Jin, Z.; Hu, R.; Wang, H.; Hu, J.; Ren, T. One-step impregnation method to prepare direct Z-scheme LaCoO<sub>3</sub>/g-C<sub>3</sub>N<sub>4</sub> heterojunction photocatalysts for phenol degradation under visible light. *Appl. Surf. Sci.* **2019**, *491*, 432–442. [[CrossRef](#)]
36. Huang, S.; Zhang, J.; Qin, Y.; Song, F.; Du, C.; Su, Y. Direct Z-scheme SnO<sub>2</sub>/Bi<sub>2</sub>Sn<sub>2</sub>O<sub>7</sub> photocatalyst for antibiotics removal: Insight on the enhanced photocatalytic performance and promoted charge separation mechanism. *J. Photochem. Photobiol. A* **2021**, *404*, 112947. [[CrossRef](#)]
37. Shangguan, X.Y.; Fang, B.L.; Xu, C.X.; Tan, Y.; Chen, Y.G.; Xia, Z.J.; Chen, W. Fabrication of direct Z-scheme FeIn<sub>2</sub>S<sub>4</sub>/Bi<sub>2</sub>WO<sub>6</sub> hierarchical heterostructures with enhanced photocatalytic activity for tetracycline hydrochloride photodegradation. *Ceram. Int.* **2021**, *47*, 6318–6328. [[CrossRef](#)]
38. Li, G.; Wang, B.; Zhang, J.; Wang, R.; Liu, H. Rational construction of a direct Z-scheme g-C<sub>3</sub>N<sub>4</sub>/CdS photocatalyst with enhanced visible light photocatalytic activity and degradation of erythromycin and tetracycline. *Appl. Surf. Sci.* **2019**, *478*, 1056–1064. [[CrossRef](#)]
39. Xu, Q.L.; Zhang, L.Y.; Cheng, B.; Fan, J.J.; Yu, J.G. S-Scheme heterojunction photocatalyst. *Chem* **2020**, *6*, 1543–1559. [[CrossRef](#)]
40. Bao, Y.J.; Song, S.Q.; Yao, G.J.; Jiang, S.J. S-Scheme photocatalytic systems. *Sol. RRL* **2021**, *5*, 2100118. [[CrossRef](#)]
41. Luo, Y.S.; Chi, Z.L.; Zhang, J.L.; Tian, B.Z. Photothermocatalytic system designed by facet-heterojunction to enhance the synergistic effect of toluene oxidation. *ChemCatChem* **2022**, *14*, e202101958. [[CrossRef](#)]
42. Wang, J.; Zhang, Q.; Deng, F.; Luo, X.B.; Dionysiou, D.D. Rapid toxicity elimination of organic pollutants by the photocatalysis of environment-friendly and magnetically recoverable step-scheme SnFe<sub>2</sub>O<sub>4</sub>/ZnFe<sub>2</sub>O<sub>4</sub> nano-heterojunctions. *Chem. Eng. J.* **2020**, *379*, 122264. [[CrossRef](#)]
43. He, R.A.; Liu, H.J.; Liu, H.M.; Xu, D.F.; Zhang, L.Y. S-scheme photocatalyst Bi<sub>2</sub>O<sub>3</sub>/TiO<sub>2</sub> nanofiber with improved photocatalytic performance. *J. Mater. Sci. Technol.* **2020**, *52*, 145–151.



44. Gogoi, D.; Makkar, P.; Ghosh, N.N. Solar light-irradiated photocatalytic degradation of model dyes and industrial dyes by a magnetic  $\text{CoFe}_2\text{O}_4\text{-gC}_3\text{N}_4$  S-scheme heterojunction photocatalyst. *ACS Omega* **2021**, *6*, 4831–4841. [[CrossRef](#)]
45. Jia, X.M.; Han, Q.F.; Liu, H.Z.; Li, S.Z.; Bi, H.P. A dual strategy to construct flowerlike S-scheme  $\text{BiOBr/BiOAc1-xBrx}$  heterojunction with enhanced visible-light photocatalytic activity. *Chem. Eng. J.* **2020**, *399*, 125701. [[CrossRef](#)]
46. Dou, L.; Jin, X.Y.; Chen, J.F.; Zhong, J.B.; Li, J.Z.; Zeng, Y.; Duan, R. One-pot solvothermal fabrication of S-scheme  $\text{OVs-Bi}_2\text{O}_3/\text{Bi}_2\text{SiO}_5$  microsphere heterojunctions with enhanced photocatalytic performance toward decontamination of organic pollutants. *Appl. Surf. Sci.* **2020**, *527*, 146775. [[CrossRef](#)]
47. Lian, X.; Xue, W.H.; Dong, S.; Liu, E.Z.; Li, H.; Xu, K.Z. Construction of S-scheme  $\text{Bi}_2\text{WO}_6/\text{g-C}_3\text{N}_4$  heterostructure nanosheets with enhanced visible-light photocatalytic degradation for ammonium dinitramide. *J. Hazard. Mater.* **2021**, *412*, 125217. [[CrossRef](#)]
48. Huang, K.J.; Zhang, J.Z.; Fan, Y. Preparation of layered  $\text{MoSe}_2$  nanosheets on Ni-foam substrate with enhanced supercapacitor performance. *Mater. Lett.* **2015**, *152*, 244–247. [[CrossRef](#)]
49. Eftekhari, A. Molybdenum diselenide ( $\text{MoSe}_2$ ) for energy storage, catalysis, and optoelectronics. *Appl. Mater. Today* **2017**, *8*, 1–7. [[CrossRef](#)]
50. Liu, Z.; Li, N.; Zhao, H.; Du, Y. Colloidally synthesized  $\text{MoSe}_2/\text{graphene}$  hybrid nanostructures as efficient electrocatalysts for hydrogen evolution. *J. Mater. Chem. A* **2015**, *3*, 19706–19710. [[CrossRef](#)]
51. Zhang, H.; Tang, G.G.; Wan, X.; Xu, J.; Tang, H. High-efficiency all-solid-state Z-scheme  $\text{Ag}_3\text{PO}_4/\text{g-C}_3\text{N}_4/\text{MoSe}_2$  photocatalyst with boosted visible-light photocatalytic performance for antibiotic elimination. *Appl. Surf. Sci.* **2020**, *530*, 147234. [[CrossRef](#)]
52. Zheng, X.T.; Yang, L.M.; Li, Y.B.; Yang, L.X.; Luo, S.L. Direct Z-scheme  $\text{MoSe}_2$  decorating  $\text{TiO}_2$  nanotube arrays photocatalyst for water decontamination. *Electrochim. Acta* **2019**, *298*, 663–669. [[CrossRef](#)]
53. Tahir, M.B.; Asiri, A.M.; Nabi, G.; Rafique, M.; Sagir, M. Fabrication of heterogeneous photocatalysts for insight role of carbon nanofibre in hierarchical  $\text{WO}_3/\text{MoSe}_2$  composite for enhanced photocatalytic hydrogen generation. *Ceram. Int.* **2019**, *45*, 5547–5552. [[CrossRef](#)]
54. Zhang, S.M.; Chen, L.; Shen, J.; Li, Z.F.; Wu, Z.H.; Feng, W.H.; Xu, K.Q.; Xu, D.F.; Chen, X.H.; Zhang, S.Y.  $\text{TiO}_2@\text{MoSe}_2$  line-to-face heterostructure: An advanced photocatalyst for highly efficient reduction of Cr (VI). *Ceram. Int.* **2019**, *45*, 18065–18072. [[CrossRef](#)]
55. Jiang, J.; Zhao, K.; Xiao, X.Y.; Zhang, L.Z. Synthesis and facet-dependent photocatalytic activity of  $\text{BiOCl}$  single-crystalline nanosheets. *J. Am. Chem. Soc.* **2012**, *134*, 4473–4476. [[CrossRef](#)]
56. Yang, S.; Shao, C.L.; Zhou, X.J.; Li, X.H.; Tao, R.; Li, X.W.; Liu, S.; Liu, Y.C.  $\text{MoSe}_2/\text{TiO}_2$  nanofibers for cycling photocatalytic removing water pollutants under UV-Vis-NIR light. *ACS Appl. Nano Mater.* **2020**, *3*, 2278–2287. [[CrossRef](#)]
57. Fan, C.; Wei, Z.; Yang, S.; Li, J. Synthesis of  $\text{MoSe}_2$  flower-like nanostructures and their photo-responsive properties. *RSC Adv.* **2014**, *4*, 775–778. [[CrossRef](#)]
58. Xiao, P.; Lou, J.; Zhang, H.; Song, W.; Wu, X.L.; Lin, H.; Chen, J.; Liu, S.; Wang, X. Enhanced visible-light-driven photocatalysis from  $\text{WS}_2$  quantum dots coupled to  $\text{BiOCl}$  nanosheets: Synergistic effect and mechanism insight. *Catal. Sci. Technol.* **2018**, *8*, 201–209. [[CrossRef](#)]
59. Liu, Y.; Zhang, P.; Tian, B.Z.; Zhang, J.L. Core-shell structural  $\text{CdS}@\text{SnO}_2$  nanorods with excellent visible-light photocatalytic activity for the selective oxidation of benzyl alcohol to benzaldehyde. *ACS Appl. Mater. Interfaces* **2015**, *7*, 13849–13858. [[CrossRef](#)]
60. Wang, S.; Han, Y.; Luo, Y.; Ma, Y.; Zhang, J.; Tian, B. Au thorn-decorated  $\text{TiO}_2$  hierarchical microspheres with superior photocatalytic bactericidal activity under red and NIR light irradiation. *J. Alloys Compd.* **2022**, *910*, 164485. [[CrossRef](#)]
61. Li, H.; Yang, C.; Wang, X.; Zhang, J.; Xi, J.; Du, G.; Ji, Z. Mixed 3D/2D dimensional  $\text{TiO}_2$  nanoflowers/ $\text{MoSe}_2$  nanosheets for enhanced photoelectrochemical hydrogen generation. *J. Am. Chem. Soc.* **2019**, *103*, 1187–1196.
62. Han, Y.Q.; Li, Q.Y.; Bao, S.Y.; Lu, Y.F.; Guan, Z.P.; Zhang, J.L.; Tian, B.Z. Z-scheme heterostructure  $\text{BiOCl-Ag-AgBr}$  with enhanced sunlight-driven photocatalytic activity in simultaneous removal of  $\text{Cr}^{6+}$  and phenol contaminants. *Catal. Today* **2021**, *376*, 151–161.
63. Guan, Z.P.; Li, Q.Y.; Shen, B.; Bao, S.Y.; Zhang, J.L.; Tian, B.Z. Fabrication of  $\text{Co}_3\text{O}_4$  and Au co-modified  $\text{BiOBr}$  flower-like microspheres with high photocatalytic efficiency for sulfadiazine degradation. *Sep. Purif. Technol.* **2020**, *234*, 116100. [[CrossRef](#)]
64. Dion, M.C.L.; Fauzia, V.; Imawan, C. The Effect of deposition of  $\text{MoSe}_2$  nanosheets on the performance of a ZnO-based UV detector. *J. Phys. Conf. Ser.* **2021**, *1951*, 012006. [[CrossRef](#)]
65. Kwon, I.S.; Kwak, I.H.; Debela, T.T.; Abbas, H.G.; Park, Y.C.; Ahn, J.; Park, J.; Kang, H.S. Se-rich  $\text{MoSe}_2$  nanosheets and their superior electrocatalytic performance for hydrogen evolution reaction. *ACS Nano* **2020**, *14*, 6295–6304. [[CrossRef](#)]
66. Wang, G.Y.; Zhang, Y.Z.; You, C.Y.; Liu, B.Y.; Yang, Y.H.; Li, H.J.W.; Cui, A.J.; Liu, D.M.; Yan, H. Two dimensional materials based photodetectors. *Infrared Phys. Technol.* **2018**, *88*, 149–173. [[CrossRef](#)]
67. Bao, S.Y.; Wang, Z.Q.; Gong, X.Q.; Zeng, C.Y.; Wu, Q.F.; Tian, B.Z.; Zhang, J.L.  $\text{AgBr}$  tetradecahedrons with co-exposed {100} and {111} facets: Simple fabrication and enhancing spatial charge separation using facet heterojunctions. *J. Mater. Chem. A* **2016**, *4*, 18570–18577. [[CrossRef](#)]
68. Hong, X.D.; Li, Y.; Wang, X.; Long, J.P.; Liang, B. Carbon nanosheet/ $\text{MnO}_2/\text{BiOCl}$  ternary composite for degradation of organic pollutants. *J. Alloys Compd.* **2022**, *891*, 162090. [[CrossRef](#)]
69. Acharya, L.; Nayak, S.; Pattnaik, S.P.; Acharya, R.; Parida, K. Resurrection of boron nitride in p-n type-II boron nitride/B-doped- $\text{g-C}_3\text{N}_4$  nanocomposite during solid-state Z-scheme charge transfer path for the degradation of tetracycline hydrochloride. *J. Colloid Interface Sci.* **2020**, *566*, 211–223. [[CrossRef](#)]

70. Tang, M.L.; Ao, Y.H.; Wang, P.F.; Wang, C. All-solid-state Z-scheme  $\text{WO}_3$  nanorod/ $\text{ZnIn}_2\text{S}_4$  composite photocatalysts for the effective degradation of nitenpyram under visible light irradiation. *J. Hazard. Mater.* **2020**, *387*, 121713. [[CrossRef](#)]
71. Cheng, C.; He, B.W.; Fan, J.J.; Cheng, B.; Cao, S.W.; Yu, J.G. An Inorganic/Organic S-scheme heterojunction  $\text{H}_2$ -production photocatalyst and its charge transfer mechanism. *Adv. Mater.* **2021**, *33*, 2100317. [[CrossRef](#)] [[PubMed](#)]
72. Deng, H.Z.; Fei, X.G.; Yang, Y.; Fan, J.J.; Yu, J.G.; Cheng, B.; Zhang, L.Y. S-scheme heterojunction based on p-type  $\text{ZnMn}_2\text{O}_4$  and n-type ZnO with improved photocatalytic  $\text{CO}_2$  reduction activity. *Chem. Eng. J.* **2021**, *409*, 127377. [[CrossRef](#)]